Published in final edited form as:
Neuroimage. 2011 October 1; 58(3): 749–760. doi:10.1016/j.neuroimage.2011.06.062.

Same-session functional assessment of rat retina and brain with manganese-enhanced MRI

David Bissig[a] and **Bruce A. Berkowitz**[a,b,*]

[a]Dept. of Anatomy and Cell Biology, Wayne State University, Detroit, MI, USA

[b]Dept. of Ophthalmology, Wayne State University, Detroit, MI, USA

Abstract

Manganese-enhanced MRI (MEMRI) is a powerful non-invasive approach for objectively measuring either retina or binocular visual brain activity in vivo. In this study, we investigated the sensitivity of MEMRI to monocular stimulation using a new protocol for providing within-subject functional comparisons in the retina and brain in the same scanning session. Adult Sprague Dawley or Long–Evans rats had one eye covered with an opaque patch. After intraperitoneal Mn^{2+} administration on the following day, rats underwent visual stimulation for 8 h. Animals were then anesthetized, and the brain and each eye examined by MEMRI. Function was assessed through pairwise comparisons of the patched (dark-adapted) versus unpatched (light-exposed) eyes, and of differentially-stimulated brain structures – the dorsal lateral geniculate nucleus, superior colliculus, and visual cortical regions – contralateral to the patched versus unpatched eye. As expected, Mn^{2+} uptake was greater in the outer retina of dark-adapted, relative to light-exposed, eyes ($P<0.05$). Contralateral to the unpatched eye, significantly more Mn^{2+} uptake was found throughout the visual brain regions than in the corresponding structures contralateral to the patched eye ($P<0.05$). Notably, this regional pattern of activity corresponded well to previous work with monocular stimulation. No stimulation-dependent differences in Mn^{2+} uptake were observed in negative control brain regions ($P>0.05$). Post-hoc assessment of functional data by animal age and strain revealed no significant effects. These results demonstrate, for the first time, the acquisition of functional MRI data from the eye and visual brain regions in a single scanning session.

Investigations of the visual system during, for example, aging or in diseases like diabetic retinopathy, typically focus on either the retina or brain. Few methods, including behavioral, electrophysiological, and positron emission tomography, have the ability to evaluate both retina and brain in the same animal and session with high resolution. This necessarily limits how the data can be understood and applied. Manganese-enhanced MRI (MEMRI) is a promising approach for addressing this limitation since it can measure function and structure of the retina or brain with high spatial resolution. MEMRI uses the paramagnetic Mn^{2+} ion as an MRI contrast agent for functional studies (e.g. Berkowitz et al., 2006; Bissig and Berkowitz, 2009; Duong et al., 2000; Eschenko et al., 2010; Kuo et al., 2006; Lin and Koretsky, 1997; Morita et al., 2002; Yu et al., 2005). Mn^{2+} preferentially enters active neurons through L-type voltage gated calcium channels, among others (Berkowitz et al., 2007b; Cross et al., 2007; Drapeau and Nachshen, 1984; Gadjanski et al., 2009), and accumulates due to the low rate of efflux from the retina (Berkowitz et al., 2007a; for modeling see Tofts et al., 2010) and brain (Chuang et al., 2009).

*Corresponding author at: Department of Anatomy and Cell Biology, Wayne State University School of Medicine, 540 E. Canfield, Detroit, MI 48201, USA. Fax: +1 313 577 3125. baberko@med.wayne.edu.

In this study, we performed three separate experiments to test the feasibility of integrating functional measurements from the retina (Berkowitz et al., 2009a; Berkowitz et al., 2006) and brain (Bissig and Berkowitz, 2009) into a single scanning session. In each study, one eye was covered with an opaque patch prior to Mn^{2+} administration and visual stimulation of awake and free-moving rats and data from several structures – the central retina, dorsal lateral geniculate nucleus (dLGN), superior colliculus (SC), and visual cortices – were collected within the same animal. This approach takes advantage of the highly lateralized rat visual system – the dLGN and primary visual cortex receive little information from the ipsilateral eye (for review, see Paxinos, 1985) – permitting functional study of the retina and brain on a within-subjects basis (Rooney and Cooper, 1988).

In the first experiment (Exp. 1), Sprague Dawley rats were investigated since our previous MEMRI studies validated a graded outer retinal response to light exposure in this strain, and good MEMRI signals from central visual structures (Berkowitz et al., 2009a; Bissig and Berkowitz, 2009). In the second experiment (Exp. 2), we repeated Exp. 1 in young-adult Long–Evans rats since both pigmented and albino rat strains are used extensively to study the visual system, but few studies have tested for differences in visual system activity between strains or through early adulthood. In the third experiment (Exp. 3), we examined approaches for improving accuracy and precision of MEMRI. Most MEMRI studies examine changes in signal intensities from T_1-weighted images. However, signal intensities can be altered by factors unrelated to tissue Mn^{2+}, like distance from the receive coil. Instead, for the retina, we compared layer-specific retinal T_1-mapping of stimulation-dependent Mn^{2+} uptake, which produces images that are independent of distance to the receive coil. For the brain, we apply Van de Moortele et al. (2009)'s ratio method for rapidly acquiring T_1-weighted images that are largely uninfluenced by several variables unrelated to Mn^{2+} uptake and tissue T_1, particularly distance from the receive coil.

Methods

Animals

In Exp. 1, Sprague Dawley rats (n=10, aged 4.6–8.7 months, weighing 302–340 g) were studied. In Exp. 2, Long–Evans rats (n=10, 1.7–2.8 months, 174–248 g) were studied. In Exp. 3, Long–Evans Rats (n=5, 3.7–5.3 months, 221–288 g) were studied. All animals were female, were housed and maintained in normal 12 h light/12 h dark cycling until the day before scanning, and were treated in accordance with the NIH Guide for the Care and Use of Laboratory Animals and the ARVO Statement on Animals in Vision Research.

Eye patch

The day before visual stimulation and MRI scanning, an opaque eye patch was adhered to one side of each animal in all three experiments. In Exps. 1 and 2, the left eye was patched in half of the subjects. In Exp. 3, the left eye was patched in three of the five subjects. Patches were made from a disk of black craft felt, sized to cover one side of the dorsal rat head, extending from the rostral edge of the external ear to the caudal vibrissae. To ensure the opacity of the patch, a smaller disk of aluminum foil, larger than the eye, was attached to the center of the felt disk with acid free tape (SuperTape; Therm O Web; Wheeling, IL). Patch placement was performed as follows: Rats were first anesthetized with diethyl ether. Puralube (Pharmaderm; Melville, New York) was applied to the selected eye. To avoid corneal abrasion, and to further reduce light exposure to the patched eye, the selected eye was then gently sutured shut with two superficial stitches per eyelid. Puralube applied over the eyelids prevented patch adhesion too close to the eye, and vibrissae on that side were clipped. The patch's foil disk was positioned over, and facing, the sutured eye, and the surrounding felt-only portions of the patch were adhered to the rat with VetBond (3M, St.

Paul, MN) or, to facilitate easier removal before scanning, a combination of eyelash glue (Andrea modlash adhesive; American International Industries, Los Angeles, CA) and spirit gum (Mehron Inc., Chestnut Ridge, NY). Rats were fit with Elizabethan collar and monitored until fully recovering from anesthesia (<15 min.). Immediately thereafter, rats were placed in darkness with free access to food and water until manganese administration on the following day. Sutures remained intact and patches remained fully adhered to all animals until scanning. Unless otherwise noted, all other experimental procedures were performed under dim red light or darkness.

Manganese injection and visual stimulation

The next day, for all three experiments, $MnCl_2$ was administered as an intraperitoneal injection (66 mg $MnCl_2 \cdot 4H_2O$/kg body weight) to awake and free-moving dark-adapted rats. Immediately afterwards, rats were placed in a visual stimulation chamber for 8 h as previously detailed (Bissig and Berkowitz, 2009). Briefly, animals were housed individually in a 32.5 cm × 32.5 cm × 17 cm tall box with four fourteen-inch computer monitors as walls. During the 8 h stimulation period, a variably rotating and processing square-wave grating with variable cycle width was simultaneously displayed on each screen using Vision Egg (v. 1.0; Straw, 2008). At the end of the 8 h stimulation period, animals were promptly prepared for MRI scanning.

In the present experiments, a white and dark-gray grating was used, with a resulting display brightness of 70 lx, as measured at the apparatus center. This setting was chosen over the 8 lx display used previously (Bissig and Berkowitz, 2009) to facilitate functional imaging of the retina: The outer retinal response to light, measured in vivo with MEMRI (Berkowitz et al., 2009b), is proportional to the logarithm of the overall light intensity. While the response of central visual structures (SC, V1, dLGN) to non-flashing patterns is somewhat reduced at higher light levels, robust responses are present even at 16,000 lx (Cooper and Allen, 1995).

MEMRI procedure

Prior to MEMRI examination, animals were anesthetized with intraperitoneal urethane injection (36% solution in 0.9% saline, prepared fresh daily; Aldrich, Milwaukee, WI). Urethane was dosed incrementally until the level of anesthesia was adequate for scanning, with Sprague Dawley rats (Exp. 1) requiring a dose of 2.2±0.2 ml/kg body weight (mean ±SD), and Long–Evans rats requiring 3.0±0.4 ml/kg in Exp. 2 and 3.4±1.1 ml/kg in Exp. 3.

In Exps. 1 and 2, MRI data were acquired on a 4.7T Bruker Avance system. MRI scanning sessions started with a whole-brain scan, performed with a whole-body transmit-only coil and a 3 cm internal diameter receive-only surface coil placed dorsal to the head, using a 3D RARE sequence (repetition time [TR] 330 ms; echo time [TE] 6.9 ms, with a RARE factor of 8, for an effective echo time of 28 ms; number of acquisitions [NA] 4; matrix size 216×248×120; field of view [FOV] 2.81 × 3.22 × 3.12 cm^3; providing a resolution of 130 μm×130 μm×260 μm; 37 min/image). Afterwards, a scan of the left eye was performed with a two-turn transmit/receive surface coil (1.0 cm diameter) placed over the eye, using a 2D adiabatic spin-echo imaging sequence (TR 350 ms; TE 16.7 ms; NA 16; sweep width 61,728 Hz; matrix size 256×512; slice thickness 620 μm; FOV 12×12 mm^2, providing and in-plane resolution of 46.8 μm (superior–inferior)×23.4 μm (axial); 23 min/image). Scanning sessions ended with a scan of the right eye, which used the same procedure as the left eye scan. For these scans, the retina was imaged in a slice intersecting the center of the lens and the optic nerve head. For Exps. 1 and 2, we also scanned a phantom roughly the size of a rat's head (containing a 10 to 1 mixture of water to 0.67 mM $MnCl_2$ in saline) using the whole-brain scanning parameters. Data from this phantom were used to model signal intensity change as a function of distance from the 3 cm surface coil.

In Exp. 3, MRI data were acquired on a 7T Bruker ClinScan system. The whole-brain scan was performed first, with a transmit-only whole body coil and a receive-only surface coil (2-element phased array for the rat brain) placed dorsal to the head, using a method recently introduced by Van de Moortele et al. (2009). In MEMRI, differential manganese uptake primarily affects tissue T_1 (Chuang et al., 2009). However, several other variables modify the signal intensity measured in standard T_1-weighted images, such as tissue proton density, distance from receive-coil, and B_1 inhomogeneity. The influence of these variables is shared by gradient echo images acquired with a small flip angle (proton density weighted, "PDGE"), and magnetization prepared rapid acquisition gradient echo (MPRAGE) images. Under the constraints described by Van de Moortele et al. (2009), MPRAGE signal intensity maps can be divided by PDGE maps, resulting in a largely-unbiased ratio map, weighted heavily by tissue T_1. In the present work, brain images were acquired with a turbo-FLASH sequence both with and without a slice-selective inversion pulse to collect MPRAGE and PDGE images, respectively, that shared almost all parameters (flip angle of 3°; TE 3.03 ms; NA 1; matrix size 192×192×128 (i.e. 112+16 for slice oversampling); echo spacing 7.77 ms; FOV 2.50 × 2.50 × 2.91 cm^3; providing a resolution of 130 μm×130 μm×260 μm). We use "$TR_{Siemens}$" and "$TI_{Siemens}$" to denote inputs to Siemens' Syngo software, which signify different parameters than TR and TI (inversion time) as sometimes used by other authors describing the turbo-FLASH sequence (e.g. McRobbie et al., 2003; Van de Moortele et al., 2009). For instance, when no inversion pulse is used, the lowest permitted setting for $TR_{Siemens}$ is the number of steps in a single phase encode step (here, 128 slices) multiplied by echo spacing (here, 7.77 ms). Acquisition time, in turn, is $TR_{Siemens}$ multiplied by the number of phase encode steps (here, 192). MPRAGE images used a $TR_{Siemens}$ of 2500 ms and a $TI_{Siemens}$ of 1500 ms (requiring 8 min/image), and PDGE images used a $TR_{Siemens}$ of 1000 ms (3 min 12 s/image). For subsequent retinal imaging, T_1 mapping was performed using the partial saturation method: Spin-echo images are acquired at several TRs, and tissue T_1 is determined with an exponential fit to the signal intensity data (described below). Using a 1.0 cm diameter receive-only coil, retinal images (TE 13, matrix size 160×320, slice thickness 600 μm; FOV 8×8 mm^2; providing and in-plane resolution of 50 μm (superior–inferior)×25 μm (axial)) were collected with each TR in the following order, and multiple single images (#) were acquired at some TRs and later averaged to improve signal-to-noise: TR 0.15 s (6), 3.50 s (1), 1.00 s (2), 1.90 s (1), 0.35 s (4), 2.70 s (1), 0.25 s (5) and 0.50 s (3).

As in previous work (Bissig and Berkowitz, 2009), whole-brain scanning began about 9 h after manganese administration, (mean (SD) for Exps. 1, 2 and 3, respectively: 8 h and 49 min (7 min); 9 h and 3 min (35 min); 8 h and 47 min (10 min)). Scans of the left eye always preceded scans of the right eye, beginning about 10 h after manganese administration (9 h and 53 min (8 min); 10 h and 12 min (37 min); 9 h and 53 min (4 min)), with scans of the right eye starting about 11 h after manganese administration (10 h and 46 min (30 min); 11 h and 7 min (44 min); 11 h and 10 min (5 min)). Rectal temperatures were continuously monitored during scanning sessions, and body temperature was maintained with a heated recirculating water system. All animals were alive throughout scanning, after which they were humanely euthanized.

Data processing: retina

The retina was processed as in previous work (Berkowitz et al., 2010): High-order polynomials spanning from ora serrata to ora serrata were fit to the provisional retina/vitreous border through a semi-automated process. Then, retinal signal intensities were sampled regularly along lines perpendicular to those polynomials, and organized as a linearized image (Fig. 1B). In Exp. 3, the images collected for each eye were registered (rigid-body) before linearization. After linearization of Exp. 3 data, a moving-window

approach (1.5 mm width) was used to ensure the retina–vitreous border (determined using the half-height method employed by Cheng et al., 2006) was well-aligned across TRs.

Retinal extent was measured from each hemiretina as the distance from the ora serrata to the optic nerve head. Linearized data were binned by % retinal extent into ten equal segments per hemiretina. For each bin, the average signal intensity (SI) as a function of retinal depth was then found (Fig. 1C). In Exp. 3, this procedure was repeated for images at each TR, and T_1 values calculated with this binned data using R (v. 2.9.0; R Development Core Team (2009); http://www.R-project.org) scripts developed in-house, and the minpack.lm library (v. 1.1.1, written by Timur V. Elzhov and Katharine M. Mullen): Using the Levenberg–Marquardt nonlinear least-squares algorithm, a 3-parameter equation was fit to SI data of each bin as a function of TR ($SI=a+b(\exp(-TR/c))$, where a, b, and c are fitted parameters, and c is the calculated T_1).

Within each data bin, the vitreous–retina, and retina–choroid borders were found with the "half height" method used elsewhere (Cheng et al., 2006; Berkowitz et al., 2009a; Berkowitz et al., 2010), and subtracted to calculate retinal thickness. In this approach, the border between adjacent structures (e.g. vitreous and retina) is found at the signal intensity midway between the local minimum (vitreous) and maximum (retina) (Fig. 1D). Linearized data were organized by distance from the vitreous–retina border according to % of the retinal thickness within each bin (Fig. 1E). In this configuration, all retinal data is spatially normalized in both dimensions (% retinal extent by % retinal thickness). Since each retinal layer occupies a similar percentage of the whole-retinal thickness throughout development and across retinal eccentricities (Braekevelt and Hollenberg, 1970), subsequent functional comparisons are straightforward.

Next, high-order polynomials were fit to the vitreoretinal border of the superior, then to the inferior, hemiretina. Retinal thickness data were then remapped on to the in situ image of the eye (Fig. 1G), and used to calculate polynomial best-fit lines for the retina/choroid border of each hemiretina. The above polynomial functions were then integrated about the central axis of the eye to estimate retinal volume and surface area.

For functional comparisons, only data from the central retina – from 10 to 30% of the total retinal extent (Figs. 1 and 2) – was analyzed. The lower limit (10% extent) was set to avoid the optic nerve head (see Fig. 2). This region was retained in the analyses of retinal structure, however, since reasonable determination of retinal borders is possible given the large size of bins, relative to the optic nerve head (Figs. 1 and 2). The upper limit (30% extent) is set for Exps. 1 and 2 to limit the influence of surface coil signal intensity gradients on functional measurements: These artifacts are caused by relative tissue distance from the surface coil, and although they are largely removed in Exp. 3 through calculation of tissue T_1, the upper limit (30% extent) is retained. Functional analysis of the periphery is also problematic given the thinness of the peripheral retina and the present image resolution. The far-peripheral retina is roughly 130 μm wide (see Results), and spatial resolution perpendicular to the peripheral retinal surface is 46.8 and 50 μm in Exps. 1,2 and 3, respectively. Therefore, a band of peripheral retinal tissue only 1 to 2 pixels wide is free of partial volume averaging with, variously, the vitreous or the choroid and sclera. This is especially relevant in Exp. 3, where accurate measurement requires that signal differences from one TR to the next mainly depend on tissue T_1. At stark structural borders, however, signal and calculated T_1 depends heavily on each tissue's exact contribution to a partial-volume average. Higher relative resolution, like in the central retina, is needed to extract meaningful layer-specific functional data.

In Exps. 1 and 2, signal intensities were muscle-normalized before paired functional comparisons of the patched and unpatched eye. Mean signal intensity (SI) was measured in three regions of muscle present in each image pair, at a similar distance from the central retina. Then, muscle signal intensities (normalized only to background noise) were compared in patched versus unpatched eyes, to check that the following step would not introduce a systematic bias: Next, muscle SIs were used to normalize retinal SIs (i.e. normalized retinal SI=retinal SI/muscle SI). Whenever signal intensities are normalized, it is also advisable to test a nearby negative control region. We therefore analyzed the identically-normalized vitreous just interior to the central retina — from 50 to 100 μm from the retina/vitreous border. For completeness, we also compare vitreous and muscle T_1 data from patched versus unpatched eyes in Exp. 3.

In all experiments, functional data (signal intensity or T_1) and structural data (thicknesses and retinal extents) from the superior and inferior hemiretinas were averaged for further analysis (Fig. 1F). This simplifies the analysis, and further reduces measurement variability due, for instance, coil position and tilt in Exps. 1 and 2. A post-hoc analysis of hemiretina-specific data was consistent with the hemiretina-averaged data that we present below (data not shown).

Data processing: brain

First, the relationship between signal intensity and distance from the surface coil was modeled with the phantom data, then used to correct signal intensities in each brain image in Exps. 1 and 2, as in Bissig and Berkowitz (2009). For each subject in Exp. 3, the PDGE image was registered to the MPRAGE image in SPM5 (http://www.fil.ion.ucl.ac.uk/spm/), then used to calculate a ratio image (MPRAGE/PDGE) (see Fig. 3). While these correction methods are imperfect, remnants of the rostrocaudal and dorsoventral components of the receive coil inhomogeneity have little influence in the present work: All analyses of the visual system, described below, compare the patched side of the rat to the unpatched side in a pairwise fashion, leaving only a mediolateral component to influence results. For this reason, the analysis of visual regions is accompanied by the analysis of several negative control regions at a similar distance from the brain midline.

As in Bissig and Berkowitz (2009), three strategies were used to analyze the functional brain data. The first of these, a whole-region of interest (ROI) analysis, was used for the dorsal lateral geniculate nucleus (dLGN) and two negative control regions: the medial geniculate nucleus (MGN) and inferior colliculus (IC). Mean values for the dLGN were calculated in MRIcro (v. 1.40, Rorden and Brett, 2000) with hand-drawn ROIs based on the rat brain atlas of Paxinos and Watson (2007). Mean values for the MGN and IC were calculated similarly using spherical ROIs (radius: 520 μm) placed in the center of each structure. In an alternative analysis, we re-examined the IC with a focus on the superficial 700 μm of that structure, using an approach similar to that applied to the superior colliculus (described below). Since statistical conclusions for this negative control region were similar in both analyses, only results from the ROI analysis are shown. All other regions of the brain were analyzed to preserve layer-specific information.

The superior colliculus (SC) was analyzed with ImageJ (Rasband, W.S., ImageJ, U. S. National Institutes of Health, Bethesda, Maryland, USA, http://rsb.info.nih.gov/ij/, 1997–2009). Signal intensities and MPRAGE/PDGE values were measured as a function of depth by hand-drawing lines perpendicular to the structure's surface (as in Silva et al., 2008; Bissig and Berkowitz, 2009) in six coronal slices (spaced evenly from, approximately, bregma −7.2 mm to bregma −5.9 mm) along six lines per slice (3 per brain hemisphere).

Analysis of neocortical regions proceeded, with slight modification, as detailed in Bissig and Berkowitz (2009). Briefly, the brain was digitally extracted from the surrounding tissue, and linearized with R scripts developed in-house. Along polynomials fit to a "silhouette" of the brain in each coronal slice, perpendicular lines were drawn every 32.5 μm. Based on the brain's contour within 390 μm×390 μm×910 μm (mediolateral×dorsoventral×rostrocaudal) area centered where each perpendicular meets its polynomial, the perpendicular lines are tilted, either rostrally or caudally, to be normal to the brain surface. Cortical data were sampled every 32.5 μm along those lines, and organized as a linearized image. To control for slight inconsistencies in the location of the linearized brain surface, a narrow moving window was used to align the brain surface near the top of each linearized image: In Exps. 1 and 2, the average signal intensity profile as a function of distance from the polynomial was found within a 812.5 μm window centered on a each line of values extracted from the original image. The provisional brain/no-brain border was found with the "half height" method (see above), and used for alignment. In experiment 3, this moving-window procedure was altered slightly. As seen in Fig. 3, and in Van de Moortele et al. (2009), ratio images will sporadically show high MPRAGE/PDGE values for tissues with very low signal intensity in both PDGE and MPRAGE images, like bone. This effect complicates direct application of moving-window procedure to ratio images. We therefore linearized the MPRAGE image with the same coordinate transform used for the ratio image, and used this to calculate the moving-window adjustments applied to the linearized ratio image.

Cortical regions of interest were selected using the digitalized version of the Paxinos and Watson (2007) rat brain atlas, which was linearized and manually aligned with the present data. R scripts developed in-house used this flattened map to calculate average profiles of signal intensity (or MPRAGE/PDGE ratio) as a function of cortical depth in two negative control regions – the primary motor cortex (M1) and forelimb region of the primary somatosensory cortex (S1FL) – and several subsets of the visual cortex: the monocular, binocular, and rostral divisions of the primary visual cortex (V1M, V1B, and V1, respectively), the lateral secondary visual cortex (V2L), and the medial secondary visual cortex (with the mediomedial and mediolateral portions analyzed as a single region, "V2M").

Excluded data

Portions of the retina were occasionally excluded from analysis because of image artifacts. In these cases, data from the artifact-free hemiretina was used in place of an average of superior and inferior hemiretina. In Exps. 2 and 3, all subjects had useable data throughout the retina from one or both hemiretinas of each eye. However, this was not true of three subjects in Exp. 1. The retinal data, but not the brain data, of these subjects were excluded from all further analysis. One subject lacked high-quality data from a small portion of the periphery from both hemiretinas of the patched eye (bin 70–80%). Only when validating retinal thicknesses at that peripheral location were this subject's data excluded. When evaluating retinal thicknesses, data from the far periphery (90–100% extent) were ignored, since partial inclusion of ora serrata and ciliary body could not be ruled out. For all subjects, functional data within 10% of the total retinal thickness from the retina/vitreous and retina/choroid borders were not analyzed due to partial-volume averaging concerns.

In Exp. 3, usable brain data could not be collected from one of the five subjects, which had the left eye patched. As in Bissig and Berkowitz (2009), no brain data falling within a 2.4 mm buffer centered at the longitudinal fissure was analyzed. For all subjects, data adjacent to the brain/no-brain border was not analyzed due to partial-volume averaging concerns. In cortical regions, data at depths corresponding to the cortical white matter and beyond was also left unanalyzed. Thus, data at depths corresponding to layers II through VI were

analyzed in each cortical region, as were the superficial gray and optic nerve layers in the SC.

Statistics

Retinal morphology—Preprocessing of the retinal data yielded, from each eye, measurements of retinal extent, surface area, volume, and whole-retinal thickness measurements as a function of % extent (i.e. eccentricity). Linear regression analyses comparing the patched to unpatched eyes were used for internal validation of each variable. Inter-individual comparisons of retinal morphology are provided as supplemental material. For all aforementioned testing, $P<0.05$ was considered significant.

Retinal function—Preprocessing of the retinal data yielded, for each eye, profiles of normalized signal intensity (and in Exp. 3, $1/T_1$) as a function of % retinal thickness. To compare manganese uptake in the patched (dark-adapted) retina versus the unpatched (light-exposed) retina, paired t-tests were performed at all points not excluded due to partial-volume averaging concerns. Given our previous rodent studies on light-dependent retinal manganese uptake (Berkowitz et al., 2009a; Berkowitz et al., 2006; Berkowitz et al., 2009b; Tofts et al., 2010), and work of others indicating that the rat outer retina is more active and ion-permeable in darkness than in light (e.g. using radiolabeled deoxyglucose, Morjaria and Voaden, 1979; and see Yau, 1994 for review) these were treated as planned one-tailed t-tests (patched>unpatched; $\alpha=0.05$). Next, the weighted Z-transform method – a meta-analytic technique for assessing significance across several tests of the same hypothesis (Whitlock, 2005) – was used to combine tests for light-dependent layer-specific retinal manganese uptake: In this approach, p-values from each of the three experiments are weighted by each test's degrees of freedom, and combined to yield a single "consensus" p-value. To coarsely relate functional data to the inner versus outer retina, the relative location of the border between the inner nuclear and outer plexiform layers was derived from published in vivo optical coherence tomography measurements (Srinivasan et al., 2006a; Srinivasan et al., 2006b). An identical statistical approach was used to compare values for the vitreous in each experiment, as well as muscle (noise-normalized signal intensities in Exp. 1 and 2, and $1/T_1$ in Exp. 3), where no differences between patched and unpatched eye were expected.

Brain function—Preprocessing of brain data yielded, for each brain hemisphere, profiles of signal intensity (and in Exp. 3, MPRAGE/PDGE ratios) as a function of depth into the cortex and SC. To compare manganese uptake in the brain hemisphere on the patched side of the head – the visually stimulated hemisphere contralateral to the light-exposed eye – to uptake in the opposite "unpatched" hemisphere, paired t-tests were performed at all points not excluded due to partial-volume averaging concerns. Whole-region means for the MGN, IC, and dLGN were analyzed in the same fashion. Given previous literature showing increases in activity during monocular visual stimulation in the dLGN, SC, primary visual cortex, and V2L contralateral to the visually-stimulated eye, (e.g. using radiolabeled deoxyglucose, Rooney and Cooper, 1988; measuring c-fos induction, Montero and Jian, 1995; using single-unit recordings Diao et al., 1983), these were treated as planned one-tailed t-tests (hemisphere ipsilateral to patchNunpatched side; $\alpha=0.05$). Data from negative control regions were tested in the same fashion. To coarsely relate functional data to histological boundaries, cortical and SC layer thicknesses were derived from previous literature and averaged as in Bissig and Berkowitz (2009) (cortex: Gabbot and Stewart, 1987; Kreig, 1946; Zilles, 1985; SC: Ortega et al., 1995; Pellegrino et al., 1979; Toga and Collins, 1981). As for the retina, tests for stimulation-dependent layer-specific retinal manganese uptake were combined across experiments using the weighted Z-transform method. Considering the abundance of planned statistical tests, we decided to highlight particularly robust statistical findings: Locations with significant functional findings below a

false-discovery rate (FDR) threshold of q=0.05 are therefore noted. FDR calculations were performed with the typical type 1 constant (i.e. c(V)=1; see Genovese et al., 2002), using the weighted Z-transform p-values calculated from all paired tests (brain and retina alike) of functional data.

Comparison of Sprague Dawley and Long–Evans rats—Visual system differences between albino and pigmented rats have been noted in previous studies. For instance, albino rats have poorer visual acuity than pigmented rats (Douglas et al., 2005; Prusky et al., 2002), and baseline glucose utilization in higher in the visual cortex of pigmented rats (Batipps et al., 1981). We used data from Exps. 1 and 2, which use identical MRI parameters, to probe for functional differences between Sprague Dawley and younger Long–Evans rats. Patched/unpatched ratios were calculated for each subject at each retinal and brain location tested. In a first-pass analysis, these data were compared between experiments with unpaired two-tailed t-tests. Further analysis used sequential regression to first assess the relationship between age and patched/unpatched ratio, and then assess any additional relationship to animal strain. For these tests, previous literature is insufficient to justify planned significance testing. Therefore, only p-values falling below an FDR threshold of q=0.05 were considered significant. Tests failing to reach this threshold, but with p-values less than 0.05, were considered marginally significant.

Results

Retinal morphology

The results of regression analyses comparing the patched to unpatched eyes are detailed in Supplemental Table 1. Briefly, good agreement was found between measurements of retina volume, extent, and surface area (all $P<0.05$). Retinal thickness measurements were well-correlated at most eccentricities (0 through 70% extent, $P<0.05$). This was not true of the far-peripheral retina, however, where the retina is thinnest, spatial resolution perpendicular to the vitreoretinal border is worst, and inter-individual differences are minimal (see Supplemental Fig. 2).

Functional retinal data

In all three experiments, the outer retina of the patched (dark-adapted) retina accumulated significantly more Mn^{2+} than in the light-exposed eye, as illustrated by signal intensity and $1/T_1$ ratios greater than 1 (Fig. 4). In Exps. 1 and 2, for much of the inner retina, Mn^{2+} uptake was no different in patched and unpatched eyes (10 to 24% thickness, $P>0.05$ within and across experiments). To facilitate comparison of strain and imaging methods used in each experiment, the maximum effect size estimate (mean of differences between patched and unpatched eye, divided by the standard deviation of those differences) found in the outer retina and inner retina alike are provided (Table 1). Consistent with expectations, no differences were found between patched and unpatched eyes at either the muscle or vitreous (for each tissue, $P>0.05$ in each experiment and across experiments).

Functional brain data

Across experiments, portions of each visual region accumulated significantly more Mn^{2+} on the patched side of the brain – contralateral to, and receiving information mainly from, the visually-stimulated eye – than on the unpatched side. This activity-dependent Mn^{2+} accumulation, illustrated by signal intensity and MPRAGE/PDGE ratios greater than 1, is shown for each experiment in Fig. 5. All locations showing significant stimulation-dependent increases in Mn^{2+} uptake, based on weighted Z-transform tests, are listed in Table 1 along with the corresponding maximum effect size estimates. The subset of region layers with results below the FDR threshold (q=0.05) is also noted in Table 1. In each

experiment, as well as in across-experiment testing, no significant differences were noted in negative control regions (IC, MGN, S1FL, M1; Fig. 6) (all $P>0.05$).

Comparison of Sprague Dawley and Long–Evans rats

We found no significant effects of age or strain (all t-tests $P>0.05$; all regression models $P>0.01$). There were few marginal results, including the outer retina where ratios tended to increase with age.

Discussion

In this study, we developed and applied a new MEMRI protocol for measuring, in a single scanning session, function of the retina and brain. In the rat, patching one eye allows for monocular visual stimulation, and provides a potentially powerful experimental design: Within-subject functional comparisons can be performed throughout the visual system — between the patched and unpatched eyes, and between brain hemispheres. Indeed, we found robust stimulation-dependent Mn^{2+} uptake in the outer retina, dLGN, throughout V2L, and most of the primary visual cortex — particularly at depths corresponding to layer IV of each sub-section of that region (V1, V1M, V1B). Consistent with expectations, no stimulation-dependent Mn^{2+} uptake was noted at negative control regions from auditory, somatosensory, and motor systems (IC, MGN, S1FL, M1). No significant differences in stimulation-dependent Mn^{2+} uptake were noted between Exps. 1 and 2 (Sprague Dawley versus Long–Evans rats). Morphological measurements from the left and right eye were well-correlated. These results underscore MEMRI as a powerful approach for investigating, in a single session, the visual system in rodents.

As expected, the outer retina demonstrated robust light-dependent Mn^{2+} uptake in each experiment. In never-patched rat and mouse models, the biological relevance of retinal Mn^{2+} uptake is well-established (Berkowitz et al., 2006; Berkowitz et al., 2009a; Berkowitz et al., 2009b; Berkowitz et al., 2010; Tofts et al., 2010). In this study, in three different experiments, in different rat strains, using different scanner settings and hardware, we again find the expected light-dependent difference in Mn^{2+} uptake at the outer retina – but not muscle, or very nearby vitreous, or Mn^{2+}-enhanced portions of the inner retina (10–22% depth) – between patched and unpatched eyes. It is therefore unlikely that an artifact of either the acquisition or processing of MEMRI data could, in all experiments, cause only some layers of the retina to systemically and significantly differ according to whether or not an eye is patched. We also note that – in contrast to the Mn^{2+}-enhanced images analyzed presently – in ongoing experiments in our lab using patched animals never injected with Mn^{2+}, baseline tissue $1/T_1$ is no higher in the retinas of patched than unpatched eyes. The results in this work are consistent with the literature: Patched/unpatched differences robustly reflect outer retinal dark/light physiology. It was therefore somewhat surprising, when combining results across experiments, that smaller but significant light-dependent Mn^{2+} uptake was also found in much of the inner retina. This contrasts with previous work in adult rodents (Berkowitz et al., 2009a; Berkowitz et al., 2009b) which consistently found no light-dependant changes in inner retinal uptake. We considered the possibility that the eye patch somehow altered the patterns of Mn^{2+} uptake in light- and dark-adapted eyes, relative to the eyes of patch-free light-adapted (PfL) or patch-free dark-adapted (PfD) adapted animals. Indeed, initial studies in our lab suggest that the patch can modestly influence retinal Mn^{2+} uptake in unpatched versus PfL eyes. Most aspects of the patching procedure nevertheless seem benign: Potential complications (e.g. change in intraocular pressure) would be equal or greater in the patched than the unpatched eye, but, importantly, we find no differences between patched and PfD eyes. We further note that no light/dark differences are detected in the inner retina when scanning takes place roughly 4 h post manganese injection – as in the studies referenced above – instead of the present 10–11 h post-injection. This applies to both

patched versus unpatched and PfL versus PfD comparisons. Thus, the present inner retinal findings seem influenced by the timing between injection and scan. The reasons for this time dependence are not clear, but may involve transport of Mn^{2+} from the dark-adapted outer to inner retina, given the rates measured in optic nerve transport (generally>2 mm/h, Watanabe et al., 2001; Olsen et al., 2010). Future investigations are warranted with data collected at different time durations post manganese injection to investigate this possibility.

In Exps. 1 and 2, differences in the distance between the surface coil and sections of the retina will introduce variability since signal intensity will be higher in tissue closer to the surface coil. Thus, quantitative comparisons of functional Mn^{2+} uptake in both central and far-peripheral retina may be influenced by such variability, although far-peripheral retina much more so than central retina. These concerns motivated our investigation of alternative acquisition methods, such as partial-saturation T_1 calculation in Exp. 3, which is independent of coil distance. In Fig. 2, several eye images are shown, which illustrate the variability in far-peripheral superior versus inferior retina (and adjacent tissues) in raw signal intensity images. While T_1 maps are free of this artifact, analysis of the far-peripheral retina would still be problematic at the present image resolution due to partial-volume averaging (see Methods, and Fig. 2 legend). In addition to the above methods choices, we believe that the present approach of averaging superior and inferior retina further minimizes such variability.

We previously used binocular visual stimulation to examine the rat brain function with MEMRI (Bissig and Berkowitz, 2009). In that study, we noted binocular stimulation-dependent Mn^{2+} uptake in layer IV of the primary visual cortex, but not at the dLGN or V2L. In previous 2-^{14}C deoxyglucose studies, all three regions responded avidly to monocular visual stimulation, (Cooper and Allen, 1995; Rooney and Cooper, 1988). We speculated that the differential findings between those studies and our past work resulted from use of monocular vs. binocular stimulation. Alternative explanations, such as the choice of animal strain or manganese dose, or regional differences in cortical Mn^{2+} uptake (e.g. Bock et al., 2009), are ruled out by the present findings of strong stimulation-dependent uptake in the dLGN and V2L in both strains. However, we did find some differences between the present MEMRI and past 2-^{14}C deoxyglucose work. Herein we report modest but significant ($P<0.05$) stimuation-dependent Mn^{2+} uptake at V2M (Table 1), where none was reported using 2-^{14}C deoxyglucose (Cooper and Allen, 1995; Rooney and Cooper, 1988). One trivial explanation is that the location of the rat primary visual cortex is known to vary from subject to subject relative to stereotaxic coordinates (Gias et al., 2005; Zilles, 1985) and the stereotaxically-defined functional regions used here included data from adjacent regions. Similarly, modest findings for some of V1M – where activity is expected to meet or exceed that of V1B (Cooper and Thurlow, 1991; Diao et al., 1983) – may represent encroachment of a quiescent V2M. An alternative explanation recognizes that the uptake of manganese and 2-^{14}C deoxyglucose represent different aspects of neuronal activity. In any event, collection of both MEMRI and 2-^{14}C deoxyglucose data from each subject could address these possibilities.

In many past MEMRI studies, only signal intensity data were collected. However, signal intensities are influenced by variables independent of neuronal activity, like distance from the receive coil. Normalizing the intensity data to adjacent tissue – either muscle (Alvestad et al., 2007; Berkowitz et al., 2010; Brozoski et al., 2007; Fa et al., 2010; Holt et al., 2010) or control brain regions (Angenstein et al., 2007; Bissig and Berkowitz, 2009) – is a common way to address this concern. However, this approach is not optimal since the corrections are imperfect and some conditions, such as aging or diabetes, may cause global, rather than region-specific, alterations in Mn^{2+} uptake, confounding data interpretation. Thus, in Exp. 3 of this study, we evaluated T_1 mapping of the retina and a recent approach to

T_1-weighted brain imaging suggested by Van de Moortele et al. (2009). In the retina, T_1 mapping yielded significant differences between the patched and unpatched eyes, with similar effect sizes to those from T_1-weighted imaging in Exps. 1 and 2 but without having to normalize the data. T_1 mapping is also applicable to the rat brain, but remains non-trivial, requiring prolonged acquisition times to achieve useful spatial resolution (Chuang and Koretsky, 2006; Chuang et al., 2009). For the brain, we found that Van de Moortele et al. (2009)'s MRPAGE/PDGE ratio technique was able to address the aforementioned problems with signal intensity data, with acceptable acquisition times, while retaining the sensitivity of MPRAGE images to tissue manganese concentrations (Lee et al., 2010). For example, we found significant stimulation-dependent Mn^{2+} uptake at the dLGN, and acceptable effect sizes in other visual regions. These results provide some justification for future study of Van de Moortele et al. (2009)'s MRPAGE/PDGE ratio approach in MEMR imaging.

In the present study, we have developed and applied several new approaches to MEMRI investigation of the retina and brain in a single subject and scanning session. The present high-resolution MEMRI measures are not limited to the visual system, and may be applied to other brain regions and sensory structures. Use of these techniques is anticipated in, for instance, longitudinal studies of aging and chronic disease, where non-invasive measurement of nervous system structure and physiology is preferred.

Supplementary materials related to this article can be found online at doi:10.1016/j.desal.2011.06.058.

Supplementary Material

Refer to Web version on PubMed Central for supplementary material.

Acknowledgments

Supported by NIH EY018109 (BAB), Juvenile Diabetes Research Foundation (BAB), NIH AG034752 (DB), Wayne State University School of Medicine MD/PhD program (DB), and an unrestricted grant from Research to Prevent Blindness (Kresge Eye Institute).

References

Alvestad S, Goa PE, Qu H, Risa Ø, Brekken C, Sonnewald U, Haraldseth O, Hammer J, Ottersen OP, HåBerg A. In vivo mapping of temporospatial changes in manganese enhancement in rat brain during epileptogenesis. Neuro-Image. 2007; 38:57–66. [PubMed: 17822925]

Angenstein F, Niessen HG, Goldschmidt J, Lison H, Altrock WD, Gundelfinger ED, Scheich H. Manganese-enhanced MRI reveals structural and functional changes in the cortex of bassoon mutant mice. Cerebral Cortex. 2007; 17:28–36. [PubMed: 16452644]

Batipps M, Miyaoka M, Shinohara M, Sokoloff L, Kennedy C. Comparative rates of local cerebral glucose utilization in the visual system of conscious albino and pigmented rats. Neurology. 1981; 31:58–62. [PubMed: 7192825]

Berkowitz BA, Roberts R, Goebel DJ, Luan H. Noninvasive and simultaneous imaging of layer-specific retinal functional adaptation by manganese-enhanced MRI. Investigative Ophthalmology and Visual Science. 2006; 47(6):2668–2674. [PubMed: 16723485]

Berkowitz BA, Roberts R, Luan H, Bissig D, Bui BV, Gradianu M, Calkins DJ, Vingrys AJ. Manganese-enhanced MRI studies of alterations of intraretinal ion demand in models of ocular injury. Investigative Ophthalmology and Visual Science. 2007a; 48(8):3796–3804. [PubMed: 17652754]

Berkowitz BA, Roberts R, Penn JS, Gradianu M. High-resolution manganese-enhanced MRI of experimental retinopathy of prematurity. Investigative Ophthalmology and Visual Science. 2007b; 48(10):4733–4740. [PubMed: 17898298]

Berkowitz BA, Gradianu M, Bissig D, Kern TS, Roberts R. Retinal ion regulation in a mouse model of diabetic retinopathy: natural history and the effect of Cu/Zn superoxide dismutase overexpression. Investigative Ophthalmology and Visual Science. 2009a; 50(5):2351–2358. [PubMed: 19074809]

Berkowitz BA, Roberts R, Oleske DA, Chang M, Schafer S, Bissig D, Gradianu M. Quantitative mapping of ion channel regulation by visual cycle activity in rodent photoreceptors in vivo. Investigative Ophthalmology and Visual Science. 2009b; 50(4):1880–1885. [PubMed: 19060264]

Berkowitz BA, Roberts R, Bissig D. Light-dependant intraretinal ion regulation by melanopsin in young awake and free moving mice evaluated with manganese-enhanced MRI. Molecular Vision. 2010; 16:1776–1780. [PubMed: 20808732]

Bissig D, Berkowitz BA. Manganese-enhanced MRI of layer-specific activity in the visual cortex from awake and free-moving rats. NeuroImage. 2009; 44(3):627–635. [PubMed: 19015035]

Bock NA, Kocharyan A, Silva AC. Manganese-enhanced MRI visualizes V1 in the non-human primate visual cortex. NMR in Biomedicine. 2009; 22(7):730–736. [PubMed: 19322808]

Braekevelt CR, Hollenberg MJ. The development of the retina of the albino rat. The American Journal of Anatomy. 1970; 127(3):281–301. [PubMed: 5436824]

Brozoski JT, Ciobanu L, Bauer CA. Central neural activity in rats with tinnitus evaluated with manganese-enhanced magnetic resonance imaging (MEMRI). Hearing Research. 2007; 228:168–179. [PubMed: 17382501]

Cheng H, Nair G, Walker TA, Kim MK, Pardue MT, Thulé PM, Olson DE, Duong TQ. Structural and functional MRI reveals multiple retinal layers. Proceedings of the National Academy of Sciences (USA). 2006; 103(46):17525–17530.

Chuang K, Koretsky A. Improved neuronal tract tracing using manganese enhanced magnetic resonance imaging with fast T_1 mapping. Magnetic Resonance in Medicine. 2006; 55(3):604–611. [PubMed: 16470592]

Chuang K, Koretsky AP, Sotak CH. Temporal changes in the T_1 and T_2 relaxation rates (ΔR_1 and ΔR_2) in the rat brain are consistent with the tissue-clearance rates of elemental manganese. Magnetic Resonance in Medicine. 2009; 61(6):1528–1532. [PubMed: 19353652]

Cooper RM, Allen K. Metabolic activity in rat visual system during exposure to high and low intensities of patterned and diffuse light. International Journal of Neuroscience. 1995; 81:27–34. [PubMed: 7775070]

Cooper RM, Thurlow GA. [2-^{14}C]Deoxyglucose uptake in rat visual system during flashing-diffuse and flashing-pattern stimulation over a 6 log range of luminance. Experimental Neurology. 1991; 113:79–84. [PubMed: 2044681]

Cross DJ, Flexman JA, Anzai Y, Sasaki T, Treuting PM, Maravilla KR, Minoshima S. In vivo manganese MR imaging of calcium influx in spontaneous rat pituitary adenoma. American Journal of Neuroradiology. 2007; 28(10):1865–1871. [PubMed: 17925377]

Diao YC, Wang YK, Pu ML. Binocular responses of the cortical cells and the callosal projection in the albino rat. Experimental Brain Research. 1983; 49(3):410–418.

Douglas RM, Alam NM, Silver BD, McGill TJ, Tschetter WW, Prusky GT. Independent visual threshold measurements in the two eyes of freely moving rats and mice using a virtual-reality optokinetic system. Visual Neuroscience. 2005; 22:677–684. [PubMed: 16332278]

Drapeau P, Nachshen DA. Manganese fluxes and manganese-dependent neurotransmitter release in presynaptic nerve endings isolated from rat brain. The Journal of Physiology. 1984; 348:493–510. [PubMed: 6325673]

Duong TQ, Silva AC, Lee SP, Kim SG. Functional MRI of calcium-dependent synaptic activity: cross correlation with CBF and BOLD measurements. Magnetic Resonance in Medicine. 2000; 43(3): 383–392. [PubMed: 10725881]

Eschenko O, Canals S, Simanova I, Beyerlein M, Murayama Y, Logothetis NK. Mapping of functional brain activity in freely behaving rats during voluntary running using manganese-enhanced MRI: implication for longitudinal studies. NeuroImage. 2010; 49(3):2544–2555. [PubMed: 19896539]

Fa Z, Zhang P, Huang F, Li P, Zhang R, Xu R, Wen Z, Jiang X. Activity-induced manganese-dependent functional MRI of the rat visual cortex following intranasal manganese chloride administration. Neuroscience Letters. 2010; 481(2):110–114. [PubMed: 20600598]

Feng L, Sun Z, Han H, Zhou Y, Zhang M. No Age-Related Cell Loss in Three Retinal Nuclear Layers of the Long–Evans Rat. 2007

Gabbot PLA, Stewart MG. Distribution of neurons and glia in the visual cortex (area 17) of the adult albino rat: a quantitative description. Neuroscience. 1987; 21(3):833–845. [PubMed: 3627437]

Gadjanski I, Boretius S, Williams SK, Lingor P, Knöferle J, Sättler MB, Fairless R, Hochmeister S, Sühs KW, Michaelis T, Frahm J, Storch MK, Bähr M, Diem R. Role of N-type voltage-dependent calcium channels in autoimmune optic neuritis. Annals of Neurology. 2009; 66(1):81–93. [PubMed: 19670438]

Genovese CR, Lazar NA, Nichols T. Thresholding of statistical maps in functional neuroimaging using the false discovery rate. NeuroImage. 2002; 15:870–878. [PubMed: 11906227]

Gias C, Hewson-Stoate N, Jones M, Johnston D, Mayhew JE, Coffey PJ. Retinotopy within rat primary visual cortex using optical imaging. NeuroImage. 2005; 24(1):200–206. [PubMed: 15588611]

Halekoh U, Højsgaard S, Yan J. The R package geepack for generalized estimating equations. Journal of Statistical Software. 2006; 15(2)

Harman AM, MacDonald A, Meyer P, Ahmat A. Numbers of neurons in the retinal ganglion cell layer of the rat do not change throughout life. Gerontology. 2003; 49:350–355. [PubMed: 14624063]

Holt AG, Bissig D, Mirza N, Rajah G, Berkowitz B. Evidence of key tinnitus-related brain regions documented by a unique combination of manganese-enhanced MRI and acoustic startle reflex testing. PloS One. 2010; 5(12):e14260. [PubMed: 21179508]

Kiyosawa I. Age-related changes in visual function and visual organs of rats. Experimental Animals. 1996; 45(2):103–114. [PubMed: 8726134]

Kreig WJ. Connections of the cerebral cortex. I. The albino rat. A. Topography of the cortical areas. The Journal of Comparative Neurology. 1946; 84:222–275.

Kuo YT, Herlihy AH, So PW, Bell JD. Manganese-enhanced magnetic resonance imaging (MEMRI) without compromise of the blood–brain barrier detects hypothalamic neuronal activity in vivo. NMR in Biomedicine. 2006; 19:1028–1034. [PubMed: 16845705]

Lee LW, So PW, Price AN, Parkinson JR, Larkman DJ, Halliday J, Poucher SM, Pugh JA, Cox AG, McLeod CW, Bell JD. Manganese enhancement in non-CNS organs. NMR in Biomedicine. 2010; 23(8):931–938. [PubMed: 20878971]

Lin YJ, Koretsky AP. Manganese ion enhances T1-weighted MRI during brain activation: an approach to direct imaging of brain function. Magnetic Resonance in Medicine. 1997; 38(3):378–388. [PubMed: 9339438]

McRobbie, DW.; Moore, EA.; Graves, MJ.; Prince, MR. MRI from Picture to Proton. Cambridge University Press; Cambridge: 2003. p. 246-249.

Montero VM, Jian S. Induction of c-fos protein by patterned visual stimulation in the central visual pathways of the rat. Brain Research. 1995; 690:189–199. [PubMed: 8535836]

Morita H, Ogino T, Seo Y, Fujiki N, Tanaka K, Takamata A, Nakamura S, Murakami M. Detection of hypothalamic activation by manganese ion contrasted T(1)-weighted magnetic resonance imaging in rats. Neuroscience Letters. 2002; 326(2):101–104. [PubMed: 12057838]

Morjaria B, Voaden MJ. The uptake of [3H]2-deoxy glucose by light- and dark-adapted rat retinas in vivo. Journal of Neurochemistry. 1979; 32:1881–1883. [PubMed: 448377]

Olsen Ø, Kristoffersen A, Thuen M, Sandvig A, Brekken C, Haraldseth O, Goa PE. Manganese transport in the rat optic nerve evaluated with spatial- and time-resolved magnetic resonance imaging. Journal of Magnetic Resonance Imaging. 2010; 32(3):551–560. [PubMed: 20815052]

Ortega F, Hennequet L, Sarria R, Streit P, Grandes P. Changes in the pattern of glutamate-like immunoreactivity in rat superior colliculus following retinal and visual cortical lesions. Neuroscience. 1995; 67(1):125–134. [PubMed: 7477893]

Paxinos, G., editor. The Rat Nervous System. Academic Press; Orlando: 1985. p. 169-221.

Paxinos, G.; Watson, C. The Rat Brain in Stereotaxic Coordinates. 6th Edition. Academic Press; Amsterdam: 2007.

Pellegrino, LJ.; Pellegrino, AS.; Cushman, AJ. A Stereotaxic Atlas of the Rat Brain. Plenum Press; New York, New York: 1979.

Prusky GT, Harker T, Douglas RM, Whishaw IQ. Variation in visual acuity within pigmented, and between pigmented and albino rat strains. Behavioural Brain Research. 2002; 136:339–348. [PubMed: 12429395]

R Development Core Team. R: A Language and Environment for Statistical Computing. R Foundation for Statistical Computing; Vienna, Austria: 2009. 3-900051-07-0http://www.R-project.org

Rooney BJ, Cooper RM. Effects of square-wave gratings and diffuse light on metabolic activity in the rat visual system. Brain Research. 1988; 439:311–321. [PubMed: 3359191]

Rorden C, Brett M. Stereotaxic display of brain lesions. Behavioural Neurology. 2000; 12:191–200. [PubMed: 11568431]

Silva AC, Lee JH, Wu CW, Tucciarone J, Pelled G, Aoki I, Koretsky AP. Detection of cortical laminar architecture using manganese-enhanced MRI. Journal of Neuroscience Methods. 2008; 167(2): 246–257. [PubMed: 17936913]

Srinivasan VJ, Ko TH, Wojtkowskt M, Carvalho M, Clermont A, Bursell S, Song QH, Lem J, Duker JS, Schuman JS, Fujimoto1 JG. Noninvasive volumetric imaging and morphometry of the rodent retina with high-speed, ultrahigh-resolution optical coherence tomography. Investigative Ophthalmology and Visual Science. 2006a; 47(12):5522–5528. [PubMed: 17122144]

Srinivasan VJ, Wojtkowski M, Fujimoto JG, Duker JS. In vivo measurement of retinal physiology with high-speed ultrahigh-resolution optical coherence tomography. Optics Letters. 2006b; 31(15): 2308–2310. [PubMed: 16832468]

Straw AD. Vision Egg: an open-source library for realtime visual stimulus generation. Frontiers in Neuroinformatics. 2008; 2:4. doi:10.3389/neuro.11.004.2008. [PubMed: 19050754]

Tofts PS, Porchiac A, Jin Y, Roberts R, Berkowitz BA. Toward clinical application of manganese-enhanced MRI of retinal function. Brain Research Bulletin. 2010; 81:333–338. [PubMed: 19524028]

Toga AW, Collins RC. Metabolic response of optic centers to visual stimuli in the albino rat: anatomical and physiological considerations. The Journal of Comparative Neurology. 1981; 199:443–464. [PubMed: 6168665]

Van de Moortele PF, Auerbach EJ, Olman C, Yacoub E, Uğurbil K, Moeller S. T1 weighted brain images at 7 Tesla unbiased for Proton Density, T2* contrast and RF coil receive B1 sensitivity with simultaneous vessel visualization. NeuroImage. 2009; 46:432–446. [PubMed: 19233292]

Watanabe T, Michaelis T, Frahm J. Mapping of retinal projections in the living rat using high-resolution 3D gradient-echo MRI with Mn^{2+}-induced contrast. Magnetic Resonance in Medicine. 2001; 46:424–429. [PubMed: 11550231]

Whitlock MC. Combining probability from independent tests: the weighted Z-method is superior to Fisher's approach. Journal of Evolutionary Biology. 2005; 18:1368–1373. [PubMed: 16135132]

Yau KW. Phototransduction mechanism in retinal rods and cones. The Friedenwald Lecture. Investigative Ophthalmology and Visual Science. 1994; 35(1):9–32.

Yu X, Ziam Y, Sanes DH, Turnbull DH. In vivo auditory brain mapping in mice with Mn-enhanced MRI. Nature Neuroscience. 2005; 8(7):961–968.

Zilles, K. A Stereotaxic Atlas. Springer-Verlag; New York: 1985. The Cortex of the Rat.

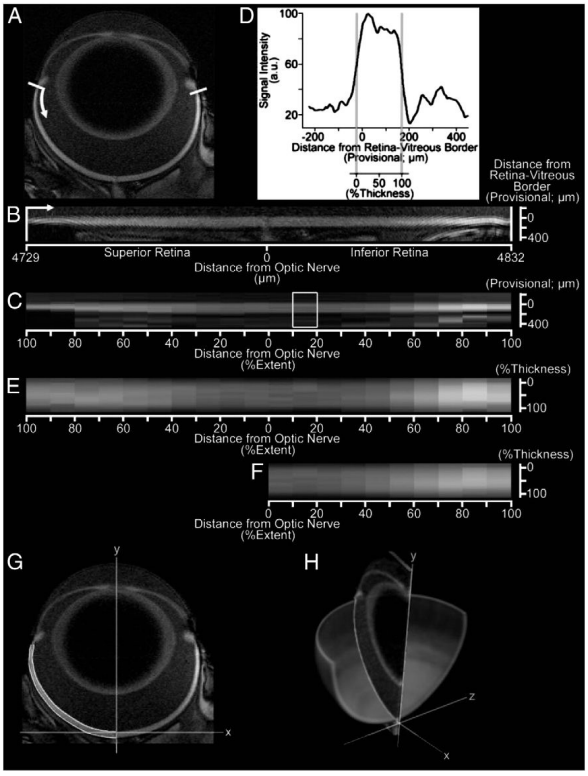

Fig. 1.

Data analysis for the retina, shown for a representative image of the eye before (A) and after (B) digital linearization of the retina (white bars and arrow provide orientation between A and B). After linearization, retinal extents – the distance from the optic nerve head to ora serrata – are measured for the superior and inferior retina. After binning retinal data in 10% increments of retinal extent (10 bins per hemiretina), mean retinal layer-specific signal intensities are found within each bin (C). Expressing the mean data for each bin as a profile of signal as a function of distance from the (provisional) retina/vitreous border (D), the retina/vitreous and retina/choroid borders are found by the half-height method (D; gray vertical lines). These borders are used to calculate retinal thickness for each bin, to estimate retinal volume (G–H), and to organize binned data as a function distance from the retina/vitreous border by % of whole-retinal thickness (E). Finally, data from the superior and inferior retina – signal intensities, as well as retinal extents and bin-specific thicknesses – are averaged for later analysis (F). For each hemiretina, a polynomial along the retina/choroid border is found after re-mapping retinal thickness data on to the original image. Polynomials for the retinal borders, shown for the superior retina in G, are integrated about central axis of the eye (H) to estimate retinal surface area and volume for each hemiretina. Note that greater signal intensities from the central towards the peripheral retina are primarily caused by the closer proximity of peripheral retina to the surface coil. Functional comparisons are restricted to the central retina (10–30% extent) in the present work.

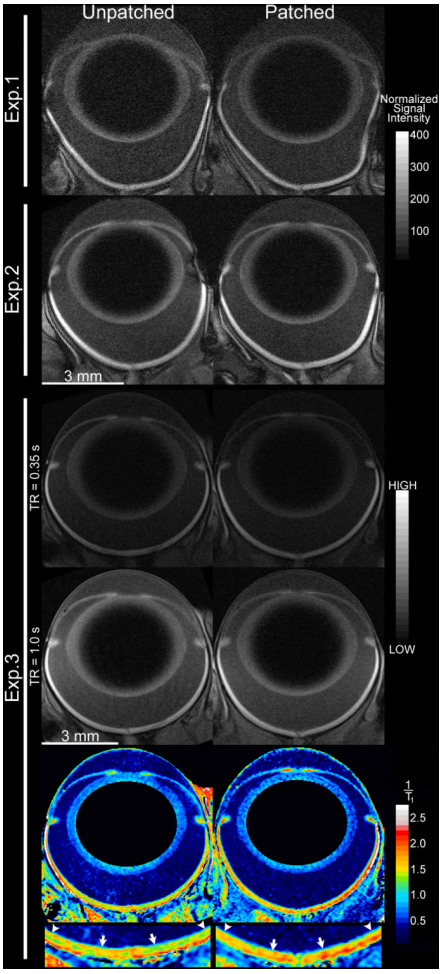

Fig. 2.

Representative images of the patched (right column) and unpatched eye from three animals. Images from Exps. 1 and 2 share the same scale bars (mm, and grays in muscle-normalized units). Grayscale images from Exp. 3 – shown for two of eight available TRs – share the same arbitrary linear units of signal intensity. $1/T_1$ maps are shown in color, in units of inverse seconds, with water-poor areas (lens center and background) masked in black. Below, the central retina (10 to 30% extent; arrows to arrowheads) of both eyes is enlarged to show contrasting patterns of inner retina, which is similar in both eyes, and outer retina, which shows lower values (blues and greens) in the unpatched than in the patched eye. A rim of high $1/T_1$ values (~2.25 s^{-1}) is visible for pixels on the border of retina with choroid (and sclera), and is an artifact of partial-volume averaging. In the analysis of central retinal function, this rim of artifact is in the excluded portion of profiles (90 to 100% depth). The artifact is exaggerated in far-peripheral retina – which is omitted from the present analyses of function – where the retina is thinnest, and image resolution perpendicular to the retinal surface is relatively low. Analysis of the iris and fine structure of the ciliary body are also susceptible to partial-volume artifacts at the present resolution, and these tissues were not evaluated in this study. In grayscale images, the higher signal intensities in the peripheral versus central retina (and adjacent vitreous) are influenced by coil proximity, as is the signal variability in far-peripheral superior (image left) versus inferior (image right) retina. These signal intensity gradients are less steep in the central retina (10–30% extent), and their influence in analysis of central retinal function is further diminished by averaging superior

and inferior retina. These signal gradients are removed when calculating $1/T_1$. Slight distortions in shape of the eye arise when the proptosed eye fits poorly within the surface coil, are most visible for the larger eyes of Exp. 1 rats (see Supplemental Fig. 1), but are unlikely to influence results: Mn^{2+} uptake reflects neuronal activity in the conscious animal prior to scanning, as evidenced by the presence of light/dark differences hours after monocular light exposure (Fig. 4), and previous tests in our lab that found no difference in Mn^{2+} uptake measurements from retinas of living versus recently-euthanized rats (unpublished data). As noted in the main text, formal calculation of retinal T_1 always followed linearization, alignment to the vitreoretinal border, and spatial normalization — the $1/T_1$ maps shown here are for display purposes only. Brain images from the same three animals are shown in Fig. 3.

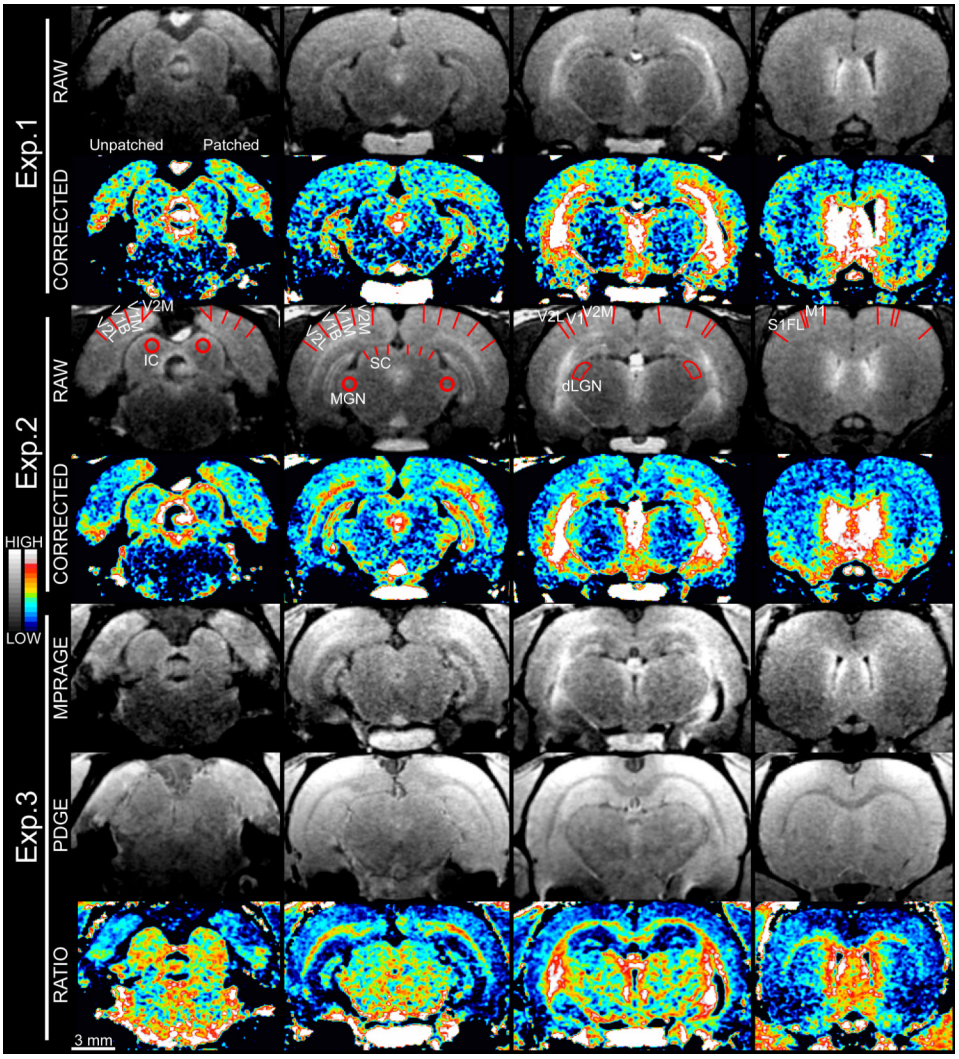

Fig. 3.

Representative brain images from three animals, both before (gray) and after (color) signal correction for distance from surface coil. The patched side of each is shown on the right side of each slice. Brain regions of interest are labeled on Exp. 2's raw images (see main text for abbreviations). SC is marked with three lines per hemisphere, representing the sampling method at that structure. Raw images use a linear gray scale of arbitrary signal units to show structural detail, while color images use a linear scale with a narrower range (scales at far left, ranging roughly ±50% and ±25% of the middle value for the gray and color scales, respectively). The narrower color range is applied to better-visualize stimulation-dependent Mn^{2+} uptake that, averaging across several slices and animals, typically amounts to a 2–3% difference in brain signal intensity (Fig. 5). As pictured, intensity comparisons are only meaningful within a series of slices from a single brain image, which are arranged from caudal (figure left) to rostral (figure right) and roughly correspond to bregma −8.8, −6.2, −4.7, and 0.4 mm (Paxinos and Watson, 2007). Negative control regions show symmetrical Mn^{2+} uptake throughout. In contrast, the dLGN, superficial SC, and portions of the visual cortex show consistently higher Mn^{2+} uptake on the patched side of the animal, which mainly receives information from the unpatched, visually-stimulated, eye. The ratio method employed for Exp. 3 results in improved white versus gray matter contrast, but this can complicate visual inspection of Mn^{2+} levels. For instance, the superficial SC clearly has

greater signal intensity on the patched than unpatched side in the MPRAGE image, but is symmetrical in the PDGE image, yielding a difference in MPRAGE/PDGE ratio consistent with expectations. This narrow band of differential uptake in the superficial gray of the SC is difficult to see in the ratio image near deeper, heavily-myelinated, midbrain structures. The mm scale at the lower-left applies throughout. Eye images from the same three animals are shown in Fig. 2.

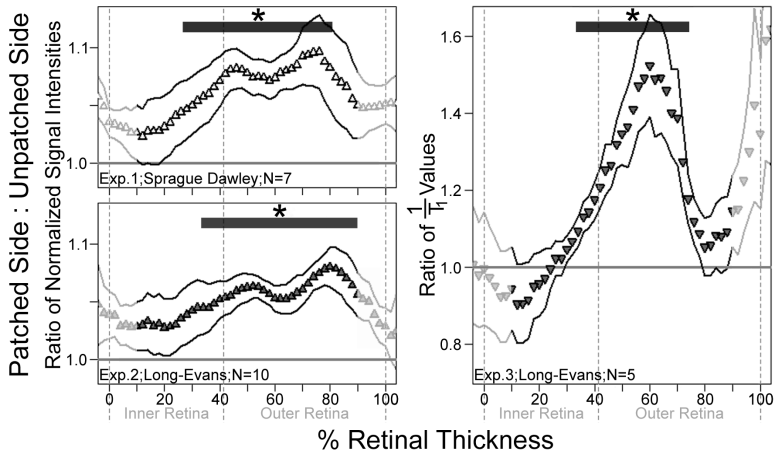

Fig. 4.

Layer-specific analysis of central (10 to 30% extent) retinal function in all three experiments. Normalized signal intensity (Exps. 1 and 2) and $1/T_1$ (Exp. 3) ratios of the patched (dark-adapted) eye to those of the unpatched (light-exposed) eye are shown. A ratio of 1.0 (horizontal line) indicates identical Mn^{2+} uptake in patched and unpatched eyes, while a ratio grater than 1.0 indicates greater Mn^{2+} uptake in the patched eye. Data are shown as a function of distance from the retina/non-retina borders, where 0 is the vitreous/retina border and 100 is the retina/choroid border. Note that the outermost retinal data (near 100%) likely includes some signal from the choroid due to partial volume averaging and other factors (Berkowitz et al., 2007a). Effect size estimates are provided for both inner and outer retina in Table 1, aiding the interpretation of the higher ratio means and variability seen in Exp. 3 (see scale). For those areas tested (from 10% to 90% of the retinal thickness), * indicates significantly greater Mn^{2+} uptake in patched eyes ($P<0.05$; paired one-tailed t-tests) at the noted depths (thick horizontal bars). Solid profile lines denote±s.e.m of ratio data.

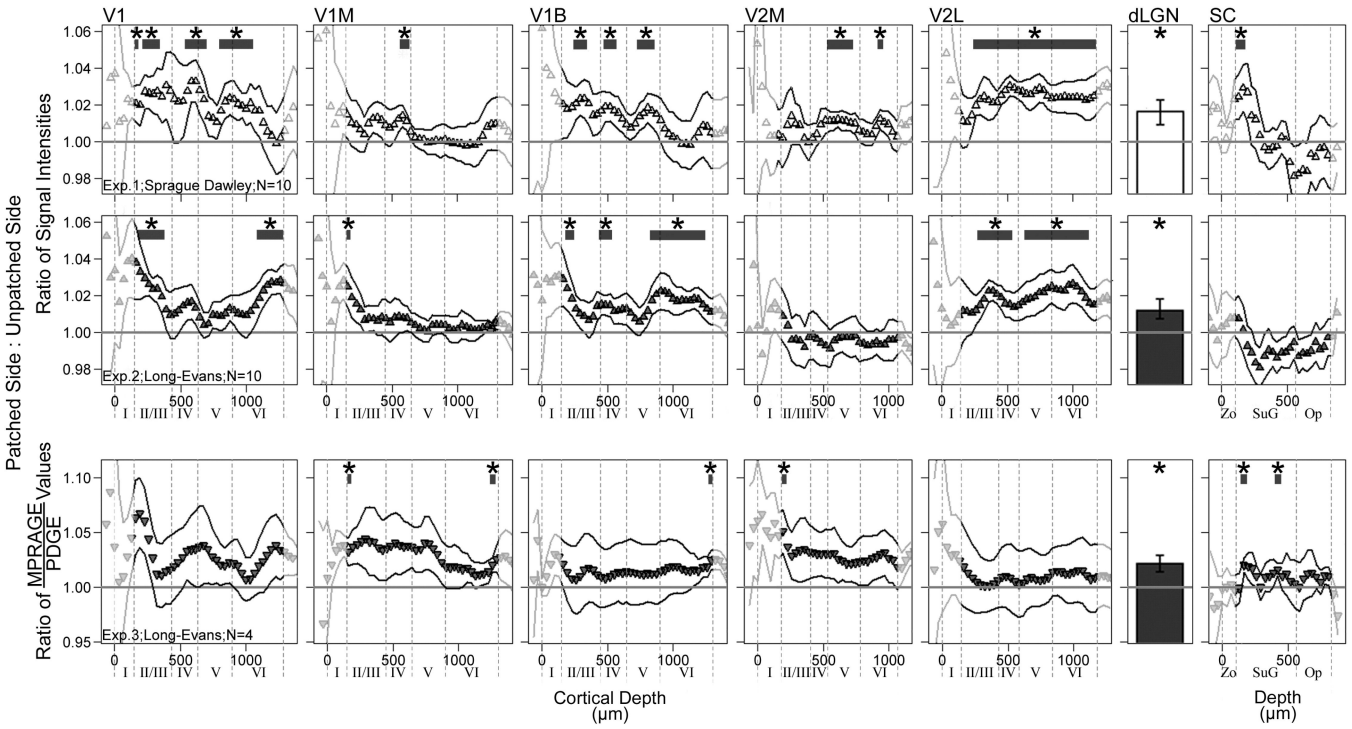

Fig. 5.

Layer-specific analysis of brain function in visual brain regions for all three experiments. Normalized signal intensity (Exps. 1 and 2) and MPRAGE/PDGE (Exp. 3) ratios of visually-stimulated brain – ipsilateral to the patch – to unstimulated brain (on the unpatched side of the head). A ratio of 1.0 (horizontal line) indicates identical Mn^{2+} uptake on each side, while a ratio grater than 1.0 indicates greater Mn^{2+} uptake in the visually-stimulated hemisphere of the brain. Profile data are shown as a function of distance from the brain/non-brain border (Cortical Depth=0). To aid in interpretation, provisional borders of cortical layers are shown (dashed lines) based on previous literature (see text). Effect size estimates are provided for all tested layers with significant weighted z-transform results in Table 1, aiding the interpretation of the higher ratio means and variability seen in Exp. 3 (see scale). For those areas tested (dLGN and undimmed portions of the profiles), * indicates significantly greater Mn^{2+} uptake on the visually-stimulated side of the brain ($P<0.05$; paired one-tailed t-tests). Solid profile lines denote±s.e.m of ratio data. Superior colliculus (SC) abbreviations: Zo — zonal layer; SuG — superficial gray; Op — optic nerve layer.

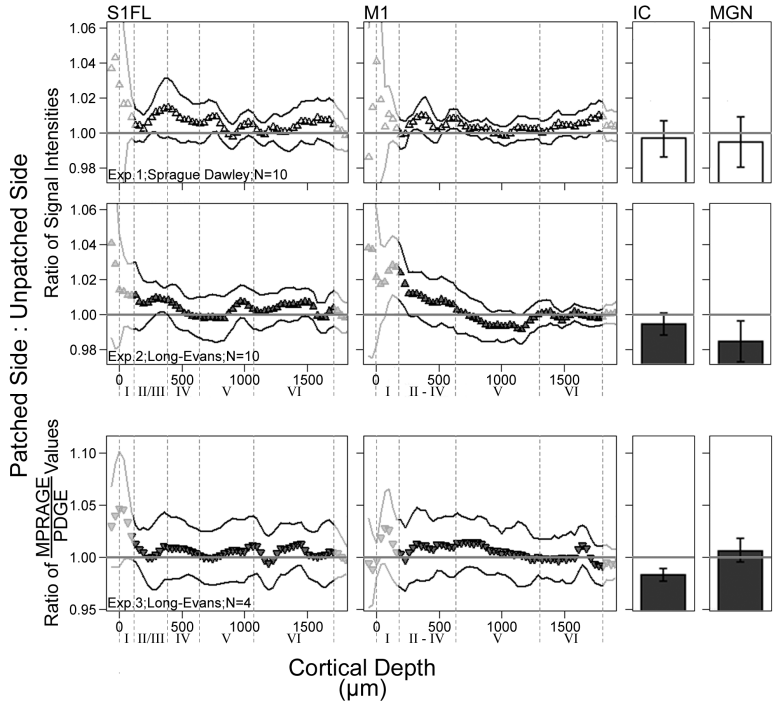

Fig. 6.

Negative-control brain regions for all three experiments. Normalized signal intensity (Exps. 1 and 2) and MPRAGE/PDGE (Exp. 3) ratios of visually-stimulated brain – ipsilateral to the patch – to unstimulated brain (on the unpatched side of the head). A ratio of 1.0 (horizontal line) indicates identical Mn^{2+} uptake on each side, while a ratio grater than 1.0 indicates greater Mn^{2+} uptake in the visually-stimulated hemisphere of the brain. Profile data are shown as a function of distance from the brain/non-brain border (Cortical Depth=0). To aid in interpretation, provisional borders of cortical layers are shown (dashed lines) based on previous literature (see text). Effect size estimates are provided for all tested layers with significant weighted z-transform results in Table 1, aiding the interpretation of the higher ratio means and variability seen in Exp. 3 (see scale). For those areas tested (IC, MGN, and undimmed portions of the profiles), * indicates significantly greater Mn^{2+} uptake on the visually-stimulated side of the brain ($P<0.05$; paired one-tailed t-tests). Solid profile lines denote±s.e.m of ratio data. Superior colliculus (SC) abbreviations: Zo — zonal layer; SuG — superficial gray; Op — optic nerve layer.

Table 1

Summary of functional data across experiments. All regions showing significant (P<0.05) stimulation-dependent changes in Mn^{2+} uptake, based on across-experiment weighted Z-transform tests, are listed. Particularly robust findings, where weighted Z-transform results fall below an FDR threshold of q=0.05 are also noted (+). To facilitate between-experiment comparisons despite unequal N's, the maximum effect size estimates from each region are provided

Region	Layer		Maximum effect size estimate		
			Exp. 1	Exp. 2	Exp. 3
Central retina	Inner	+	1.24	1.12	1.57
	Outer	+	1.83	2.52	1.89
dLGN	-	+	0.70	0.74	1.46
SC	SuG		0.73	0.12	1.71
V1	II/III	+	0.96	1.44	1.02
	IV	+	0.95	0.52	0.62
	V	+	0.80	0.56	0.57
	VI	+	0.91	1.34	0.67
V1B	II/III	+	0.82	0.60	0.48
	IV	+	0.75	0.88	0.23
	V	+	0.73	0.77	0.22
	VI		0.29	1.06	1.33
V1M	II/III		0.51	0.71	1.28
	IV	+	0.75	0.34	0.84
	V		0.39	0.29	0.95
V2M	V		0.95	−0.04	0.69
V2L	II/III	+	1.14	1.46	0.24
	IV	+	2.05	0.94	0.15
	V	+	1.49	0.79	0.16
	VI	+	1.03	0.88	0.28